Journal of Biomedical Optics

BiomedicalOptics.SPIEDigitalLibrary.org

Birefringence of a normal human red blood cell and related optomechanics in an optical trap

Belavadi Venkatakrishnaiah Nagesh
Yogesha
Ramarao Pratibha
Praveen Parthasarathi
Shruthi Subhash Iyengar
Sarbari Bhattacharya
Sharath Ananthamurthy

SPIE.

Birefringence of a normal human red blood cell and related optomechanics in an optical trap

Belavadi Venkatakrishnaiah Nagesh,[a,b] Yogesha,[a] Ramarao Pratibha,[c] Praveen Parthasarathi,[a] Shruthi Subhash Iyengar,[a] Sarbari Bhattacharya,[a] and Sharath Ananthamurthy[a,*]
[a]Bangalore University, Department of Physics, Jnanabharathi, Bangalore 560056, India
[b]M.S. Ramaiah Institute of Technology, Department of Physics, M.S.R. Nagara, Bangalore 560054, India
[c]Raman Research Institute, Soft Matter Division, C.V. Raman Avenue, Bangalore 560080, India

Abstract. A normal human red blood cell (RBC) when trapped with a linearly polarized laser, reorients about the electric polarization direction and then remains rotationally bound to this direction. This behavior is expected for a birefringent object. We have measured the birefringence of distortion-free RBCs in an isotonic medium using a polarizing microscope. The birefringence is confined to the cell's dimple region and the slow axis is along a diameter. We report an average retardation of 3.5 ± 1.5 nm for linearly polarized green light ($\lambda = 546$ nm). We also estimate a retardation of 1.87 ± 0.09 nm from the optomechanical response of the RBC in an optical trap. We reason that the birefringence is a property of the cell membrane and propose a simple model attributing the origin of birefringence to the phospholipid molecules in the lipid bilayer and the variation to the membrane curvature. We observe that RBCs reconstituted in shape subsequent to crenation show diminished birefringence along with a sluggish optomechanical response in a trap. As the arrangement of phospholipid molecules in the cell membrane is disrupted on crenation, this lends credence to our conjecture on the origin of birefringence. Dependence of the birefringence on membrane contours is further illustrated through studies on chicken RBCs. [DOI: 10.1117/1.JBO.19.11.115004]

Keywords: birefringence; biomedical optics; microscopy.

Paper 140499PRR received Aug. 1, 2014; accepted for publication Oct. 22, 2014; published online Nov. 14, 2014.

1 Introduction

A normal human red blood cell (RBC) is discotic in shape with a diameter of ~8 μm. It has a thickness of ~2 μm at the rim and ~1 μm at the dimple region. One of the major functions of an RBC, which is to transport oxygen to different parts of a human body, is linked intricately to its shape, size, and mechanical properties. Available literature[1–11] indicates much effort to understand the structure, mechanical, and viscoelastic properties of the RBC. There remain, however, several aspects of the RBC structure that are yet to be completely understood, a case in point being the biconcave shape of the RBC and the dynamic fluctuations of its membrane. Some studies link these to the presence of adenosine triphosphate (ATP),[4,7] while others contradict this claim.[5]

A perusal of available literature shows that the optical tweezer has played a pivotal role in elucidating the mechanical properties of the RBC membrane. It is also known that the dynamical behavior of a micro-object in an optical tweezer is strongly linked to its shape and birefringence.[12,13] It was demonstrated by Cheng et al.[14] that a linearly polarized tweezer can rotationally trap a birefringent microdisk. RBCs on entering an optical trap are found to reorient, acquiring an edge-on orientation with respect to the beam propagation direction. This reorientation can be explained on the basis that asymmetric micro-objects in an optical tweezer orient such that maximum of their volume lie in the region of the highest electric field. Further, in the case of a linearly polarized tweezer, RBCs tilt about an axis parallel to the electric field direction of the trapping laser and remain rotationally bound to the plane of polarization of the incident light after the reorientation. This is a clear indication that RBCs are birefringent objects.

Nonetheless, a survey of literature indicates a paucity of recent work that addresses the optical properties of RBCs. An earlier work, in 1969, by Srivastav and Burton[15] reports an observation indicating the presence of birefringence in RBCs without, however, a quantitative measure of the birefringence. They conjecture that the biconcave shape of the RBC is due to protein chains present across the cell at the dimple region and also attribute the birefringent property to this. This, however, is untenable in the light of later studies.[11] Perutz and Mitchison[16] in their studies report the presence of birefringence in sickle-celled RBCs. They attribute this to crystallized structures of hemoglobin and, consequently, expect to see no birefringence in RBCs. Ponder and Barreto[17] have reported that only ghost cells of RBCs that contain enough residual hemoglobin to be visible under a microscope show a measurable birefringence. Mitchison[18] has reported that the RBC membrane does not show birefringence in saline but shows a negative birefringence in glycerol. Ghosh et al.[19] have claimed that an RBC folds when trapped and so exhibits form birefringence. It is, thus, clear that apart from the work of Srivastav and Burton,[15] birefringence has never been attributed to undistorted RBCs.

There is an opinion that birefringence-based structural analysis of biological cells is better than other methods, like electron microscopy or x-ray analysis, for studying cells in their native

*Address all correspondence to: Sharath Ananthamurthy, E-mail: asharath@gmail.com

0091-3286/2014/$25.00 © 2014 SPIE

states.[20] With a view to enabling an alternate route to understanding the structure and dynamical behavior of RBCs using birefringence measurement as a tool, we have carried out this study where we report a measurement of the birefringence of an undistorted RBC suspended in phosphate buffered saline (PBS) using a polarizing microscope. Further, we estimate the RBC birefringence from optical tweezer based studies of the time required for realignment of the trapped RBC when the plane of polarization of the trapping laser is rotated using a half wave plate. We find that this estimate is indeed within the range of the value obtained from polarizing microscope based measurements. We also show here that the measured RBC birefringence compares with birefringence values reported for various phospholipids. We, thus, link the origin of the birefringence in the RBC to the phospholipid content of the lipid bilayer in the RBC membrane and further substantiate this by showing that the variation in birefringence measured over the RBC surface can be explained by the variation in relative orientation of the phospholipid molecules in the RBC membrane assuming a simple geometrical model for the biconcave shape of the RBC. We also report that RBCs restored in shape subsequent to a process of crenation show diminished to no measurable birefringence using a polarizing microscope along with an altered optomechanical response of sluggish reorientation in an optical trap. As the process of crenation disrupts the original alignment of the phospholipid molecules in the membrane, with this study, we lend further credence to a sensitive dependence of the birefringence on the relative orientation of phospholipid molecules in the RBC membrane. Finally, we use the study of birefringence of chicken RBC where the membrane curvature is clearly different from that in a human RBC to further endorse the view that the birefringence indeed has its origin in the phospholipid content of the cell membrane with a sensitive dependence on the alignment of phospholipid molecules that is dictated by the membrane contour.

This study could, thus, be viewed as paving the route to a noninvasive method of understanding the structure of the RBC membrane. The birefringence variation over the RBC volume can provide clues about the possible orientations of the phospholipids in the membrane. This could, in turn, provide us new insights into the biconcave structure. The variation in the birefringence is also capable of marking out the position of the RBC dimple. Variations of this, both temporally as well as spatially, could help in the study of RBC membrane fluctuations and provide further clues to its link with the mechanical properties of the RBC as well as the presence of ATP.[4,5,7]

2 Materials and Methods

2.1 *Materials*

Fresh blood drawn by the finger prick method from healthy donors is taken in a tube containing Ethylenediaminetetraacetic acid, an anticoagulant and diluted with PBS. This solution is taken in an appropriate quantity so that the absorption of light by the buffer is minimal and is held in an O-ring stuck on a glass slide.

About 100 cells each from five healthy individuals of varying demography within Asia and in the age group of 20 to 40 years have been analyzed. However, the statistical analyses presented are carried out with blood samples collected (at various instances spanning across a year) primarily from one healthy individual. The observations made across different blood samples are found to be similar in all aspects of birefringence reported.

2.2 *Methods*

2.2.1 *Identification of the slow axis*

Observations are made on the suspended RBCs between crossed polarizers under a polarizing microscope (ORTHOLUX II POL-BK, Leitz, Germany) along with a full wave (547 nm) retardation plate, the latter being useful in determining the orientation of the slow axis. When viewed under white light illumination between crossed polarizers, the full wave retardation plate exhibits first-order red (magenta). When a birefringent specimen is introduced into the optical path such that the slow axis of the retardation plate and the specimen are parallel, the relative retardation increases, resulting in a shift to longer wavelengths and a second-order blue interference color appears (see schematic Fig. 1). On the other hand, if the slow axis of the retardation plate and the specimen are perpendicular to each other, the relative retardation decreases shifting toward shorter wavelengths and the specimen exhibits first-order yellow interference color.

In order to identify the slow axis of the RBC, it is necessary to orient the principal axis, which is along a diameter[15] at 45 deg with respect to both the analyzer and polarizer, as shown in Fig. 3(a). As the RBCs are in a liquid medium, it is difficult to fix the orientation of all the RBCs present in the buffer solution along a fixed direction. We have, therefore, carried out our measurements by choosing those RBCs that are oriented in the appropriate position, i.e., edge-on to the beam propagation direction with the plane of the RBC tilted 45 deg with respect to the axes of both polarizer and analyzer. The full wave

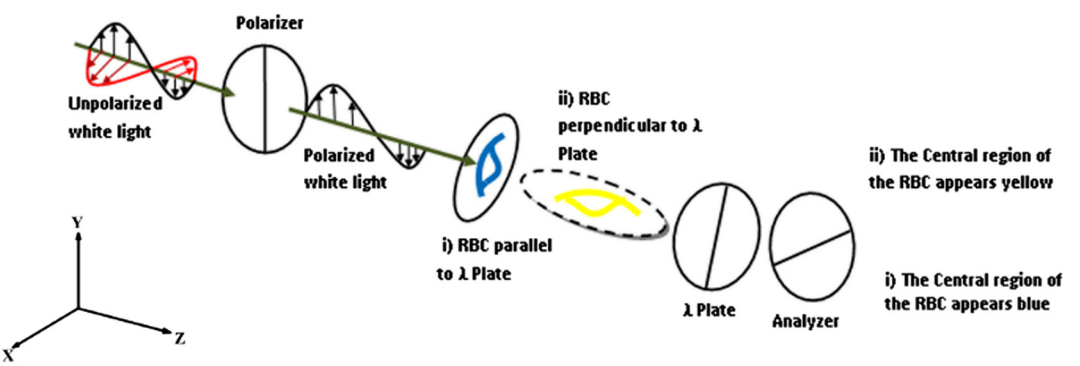

Fig. 1 Schematic for identification of the slow axis.

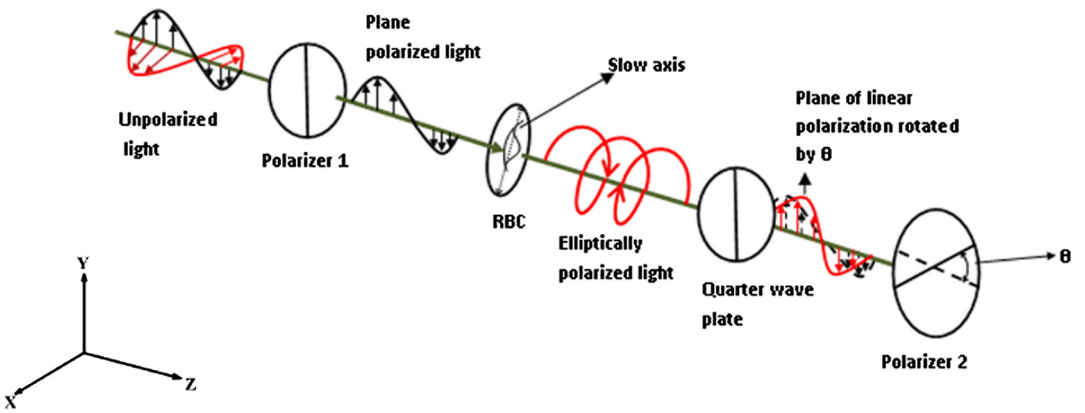

Fig. 2 Schematic for Sénarmont technique.

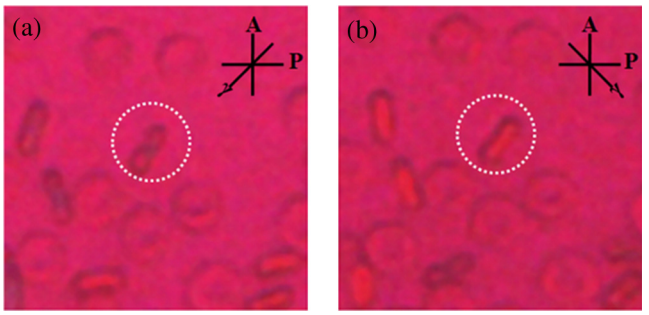

Fig. 3 Identification of slow axis. Central region of the RBC appears (a) blue if its diameter is parallel to the slow axis of the lambda plate and (b) yellow if its diameter is perpendicular to the slow axis of the lambda plate. The background remains magenta, indicating the absence of any birefringence of the buffer solution. In order to increase visibility, the contrast has been increased identically on both photographs.

retardation plate is then introduced into the optical path such that its slow axis is either parallel or perpendicular to the diameter of the RBCs.

2.2.2 *Measurement of the birefringence (Sénarmont technique)*

Subsequent to identifying the slow axis of the RBCs, the birefringence is measured using the Sénarmont technique[21] (see schematic Fig. 2). Light from a mercury vapor lamp passing through a green filter resulting in a wavelength range of 556 ± 55 nm is used for the Sénarmont technique based retardation measurements. The measurements are carried out using a quarter wave plate for a wavelength of 546 nm. The wavelength of the incident light was appropriately chosen by a suitable filter (PanchromGrun, Leitz). As described earlier, the polarizer and analyzer are kept in the crossed condition. RBCs oriented edge-on to the beam propagation direction with their diameters at 45 deg (clockwise or anticlockwise) to the electric vector of the incident light beam are chosen for the measurements. The process of imaging the RBCs took a maximum of 5 min. Only those RBCs that did not change their orientations during the measurement process were used for our calculations. Note, however, that it was made certain that the RBCs could change their orientation easily with slight disturbances, clearly indicating that they were freely suspended in the PBS and could be assumed to be undistorted in shape. On passing through the RBC, the outgoing beam consists of two linearly polarized components of equal amplitude. One of the components is phase shifted by $2\pi t\Delta\mu/\lambda$ with respect to the other. Here t, λ, and $\Delta\mu$ are the optical path length, wavelength of the incident light, and the birefringence, respectively. These two components are then made to pass through a quarter wave plate arranged with its slow axis parallel to the polarizer, resulting in two opposite circularly polarized beams. Superposition of these two beams results in a linearly polarized beam whose vibration direction is now rotated by $\pi t\Delta\mu/\lambda$ with respect to the vibration direction of the incident beam. If the analyzer is now rotated by an angle $\theta = \pi t\Delta\mu/\lambda$, the intensity should become null. This angle θ, called the angle of extinction, can be used to extract the value of the birefringence $\Delta\mu$. Here we plot the change in intensity at the center of appropriately oriented RBC as a function of the angle between the polarizer and analyzer to estimate the angle of extinction or analyzer compensation. We report values of retardation, which is the product of the optical path length in the sample with the birefringence ($t\Delta\mu$). The retardation was computed from the analyzer compensation using the equation

$$\text{Retardation} = (546\ \text{nm} \times \text{analyzer compensation})/180\ \text{deg}. \quad (1)$$

The images of the RBCs were digitally recorded (Olympus, C4000, 3X Optical zoom, 4 Mega pixel) for various angles of rotation of the analyzer.

3 Results and Discussion

3.1 *Slow Axis Identification*

Our observations show that when the diameter of the RBC is oriented parallel to the slow axis of the full wave plate, the center of the RBC appears blue. On the other hand, when the wave plate is oriented such that its slow axis is orthogonal to the diameter of the RBC, the center of RBC appears yellow. The surrounding buffer solution always exhibits a first-order magenta, indicating the absence of birefringence. The edge of the RBC appearing similar to the background may be due to the diminished birefringence here [Figs. 3(a) and 3(b)]. These observations indicate that the RBCs are indeed birefringent and that the slow axis is along a diameter of the RBC.

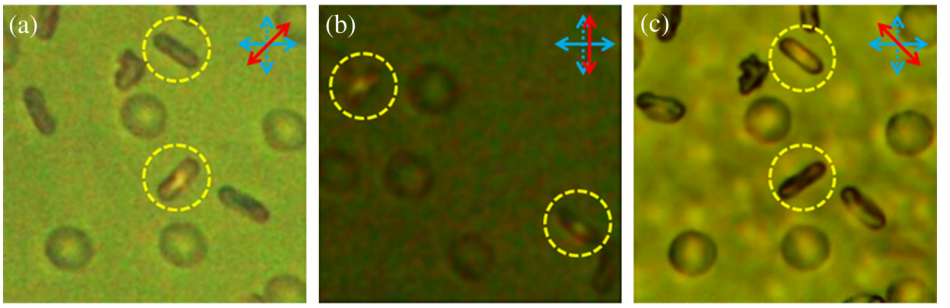

Fig. 4 Images recorded for RBCs with edge on orientation to beam propagation direction between crossed polarizers of a polarizing microscope with a quarter wave plate introduced between sample and analyzer such that its slow axis is parallel to the polarizer axis. The images have been recorded under green light illumination ($\lambda = 546$ nm) for various angles between polarizer and analyzer. (a) Image recorded at an angle where $RBC_{+45\ deg}$ is dark, while the center of $RBC_{-45\ deg}$ is bright. (c) Image recorded at an angle where the center of $RBC_{+45\ deg}$ is bright, while $RBC_{-45\ deg}$ is dark. (b) An intermediate angle where RBCs of both orientations show bright centers. The angles at which each of the images [4(a), 4(b), and 4(c)] have been recorded have been indicated with arrows on the *X* axis of the plot in Fig. 5. Also note the change in the background intensity indicating the change in the angle between the analyzer and polarizer. In order to increase visibility, the contrast has been increased identically on all three photographs.

3.2 *Birefringence Measurement Using Polarizing Microscope*

Image analysis was carried out on the recorded images of several RBCs oriented in the appropriate direction for various angles between the polarizer and analyzer using ImageJ. Figure 4 shows a set of images recorded at different angles between the analyzer and polarizer. It can be seen from Fig. 4(a) that an RBC oriented with its slow axis at 45 deg clockwise to the polarizer direction ($RBC_{+45\ deg}$) is dark, while an orthogonally oriented one (slow axis at 45 deg anticlockwise to the polarizer direction, $RBC_{-45\ deg}$) has a bright center. Figure 4(c), on the other hand, is recorded at an angle where $RBC_{+45\ deg}$ has a bright center, while the orthogonally oriented one ($RBC_{-45\ deg}$) is dark. Figure 4(b) is at an intermediate angle where the center of RBCs of both orientations appears bright. Since the cells were freely suspended, they did not maintain their orientation for times >30 s. Therefore, the same set of cells has not been imaged in Figs. 4(a), 4(b), and 4(c). Variation in intensity at the center of $RBC_{+45\ deg}$ as a function of the angle between the polarizer and analyzer is shown in Fig. 5 along with that of $RBC_{-45\ deg}$ as well as the background. A Malus law fit was carried out for each of the intensity variations and the shift in the minima of the curve corresponding to the RBC intensity with respect to that for the background gives us the analyzer compensation. The estimated retardations have been shown in Table 1.

It should be remarked here that wavelength-dependent anisotropic absorption of the composites of aligned biomolecules leading to dichroism can, in principle, appear as birefringence, especially in situations where the measured birefringence is small.[22] The retardation measured could, therefore, have contributions from possible dichroism over and above the birefringence. We have not attempted to estimate the contribution due to dichroism here. Of significance here is the nature of the optomechanical response of the RBC in a polarized optical trap that is a clear indication of its birefringence.[12,23] The reported retardation is to be regarded, therefore, as an upper bound estimate for the birefringence and not a precision measurement.

The intensity profile corresponding to the RBCs under crossed polarizers [Fig. 6(b)] shows a maximum at the center

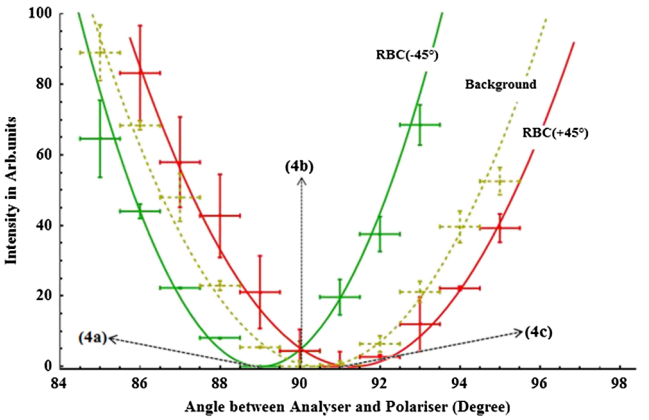

Fig. 5 Variation in intensity at the center of $RBC_{+45\ deg}$, $RBC_{-45\ deg}$, as well as the background as a function of angle between the polarizer and analyzer. The continuous curves are Malus law fits for each of the intensity variation. The analyzer compensation is estimated from the shift in the minima of the curve corresponding to the RBC intensity from that of the background. The arrows indicate the angle at which the image corresponding to the arrow label was recorded.

of the dimple region decreasing toward the ends of the dimple region.

3.3 *Birefringence Estimate from the Optomechanical Response of an RBC in an Optical Trap*

In our optical tweezer setup, light from an Ytterbium fiber laser with a wavelength range of 1064.586 ± 0.318 nm was used in experiments studying the optomechanical response of the RBC. The details of trapping an RBC are explained elsewhere.[23] The observations carried out with the polarizing microscope corroborate with results from our experiments using an optical tweezer. When an RBC is trapped in a linearly polarized optical trap, the RBC tilts and reorients with the normal to the disc perpendicular to the laser beam.[23] When RBCs are trapped using an unpolarized laser beam, the choice of axis about which the reorientation occurs (tilt axis) is random, i.e., there

Table 1 Summary of all the results discussed in this section.

Type	Method employed	Retardation measured
Normal human RBC	Polarizing microscope	$RBCs_{+45\ deg}$
	Fit to intensity change as the angle between polarizer and analyzer is varied	4 ± 1.5 nm
		$RBCs_{-45\ deg}$
		3 ± 1.5 nm
	Optical tweezer	1.87 ± 0.09 nm
	Fit to variation in angular displacement with time for the process of realignment	
Reformed RBC	Polarizing microscope	Varies between 0 and 1.5 nm
	Angle of complete extinction	
Chicken RBC	Polarizing microscope	3.5 ± 1.5 nm
	Angle of complete extinction	

is no preferential axis of tilt. In a linearly polarized tweezer, however, the tilt axis is found to be always parallel to the electric field vector of the laser beam. Further, the RBC remains rotationally bound to the direction of the electric field polarization of the laser beam after the reorientation. Throughout we find no evidence of any folding.

The reorientation of the RBC to acquire an edge-on orientation to the beam direction occurs so that the maximum of its volume lies in the region of the highest electric field. The rotationally bound behavior of the RBC, on the other hand, is explained in terms of the slow axis of the RBC, which lies along a diameter, getting locked along the electric field direction of the linearly polarized laser beam. This is as expected for a negative birefringent object.[12,13] When the slow axis of an RBC makes an angle θ with the plane of vibration of the incident electric field, the state of polarization is changed to elliptical polarization, resulting in a torque in the opposite direction to the sense of polarization in order to conserve momentum. This change in the state of polarization ceases once the slow axis of the birefringent object aligns parallel to the electric field direction. Therefore, a birefringent object trapped by a linearly polarized laser beam orients such that its slow axis is parallel to the electric field of the polarized light.

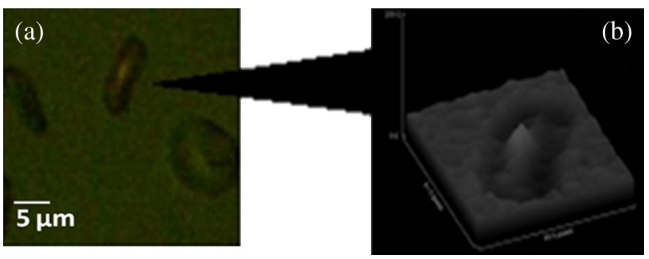

Fig. 6 RBC exhibiting birefringence. (a) RBC between crossed polarizers and under green light illumination ($\lambda = 546$ nm). (b) Surface intensity profile of the RBC viewed edge-on. The intensity confined to the dimple region is maximum at the center and reduced toward the ends.

The reoriented RBC, whose slow axis is now locked along the electric vector of the linearly polarized beam, follows the direction of the electric vector when the latter is changed by introducing a $\lambda/2$ plate in the optical path. A recording of such a realignment process at a laser power of 4 mW is shown in Fig. 7. Such realignment processes were recorded at a wide range of laser powers. The variation of the orientation of the RBC as a function of time extracted from a video recording of the realignment process at 28 mW is shown in Fig. 8. We use an expression for the alignment torque experienced by a birefringent object in such situations[12,13] and apply it in the rotational equation of motion for a rigid disk under a low Reynold's number condition as shown below.

$$\frac{32}{3}\eta r^3 \frac{d\theta}{dt} = -\frac{P}{\omega} \sin\left(360 \times \frac{R}{\lambda}\right) \sin 2\theta. \quad (2)$$

Here, θ is the angular displacement (angle between slow axis of the RBC and the plane of polarization of the incoming beam), t is the time, η is the viscosity of the surrounding medium, r is the radius of the RBC, P is the laser power at the sample plane, ω is the angular frequency, R is the retardation, and λ is the wavelength of the laser light. Fitting the experimentally observed variation of angular displacement with time using Eq. (2) yields a value of 1.87 ± 0.09 nm for the retardation. This is in a reasonable range of the measurements made using the polarizing microscope. Discrepancy between this value and that from polarizing microscope based measurements could be due to several contributory factors, such as the assumption that the RBC is a perfectly rigid disk in the rotational equation of motion, limited frame rate of the camera, or large least count for the angular measurement of the analyzer of the polarizing microscope as well as the possible presence of dichroism in the RBC.

High-speed edge-on rotations of birefringent microdisks in an optical tweezer have been demonstrated with the use of circularly polarized light. In the case of the RBCs, the maximum possible rotational torque[12,13] under circularly polarized light estimated using the value of retardation we have measured is small at the laser power range we use. Consequently, we can expect to see the fastest rotations at the rate of one complete rotation in ~3 h. Observing a sustained rotation at such slow rates is difficult considering the experimental conditions in the tweezer.

3.4 *Origin of Birefringence in the RBC*

Our measurements show that the birefringence is confined to the dimple region of the RBC. Hemoglobin or other constituents of the cytoplasm are uniformly spread over the RBC volume and are, therefore, present in larger quantities at the rim than at the dimple. Thus, these components cannot be the cause of the birefringence observed. We, therefore, associate the origin of the birefringence with the membrane. The RBC membrane consists of a fluid lipid bilayer with an underlying two-dimensional cytoskeleton network of spectrin molecules having short actin filaments and some proteins at the nodes, along with certain transmembrane proteins that bind the two together.[6,24] While several components in the human RBC are optically anisotropic in nature and can contribute to birefringence, barring the phospholipid content of the lipid bilayer, none of them exhibit

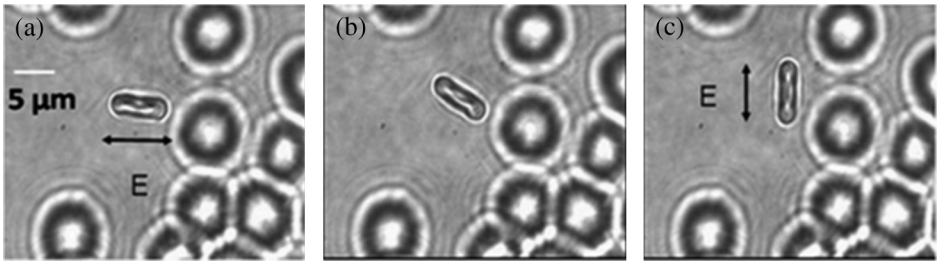

Fig. 7 Reorientation of trapped RBC using a $\lambda/2$ plate. The arrows indicate the direction of the linear polarization of laser. (a) [time: 0 s], (b) [time: 4.63 s] and (c) [time: 9.25 s] are time sequential images of the reorientation process

any kind of spatial long-range orientational alignment, which is extremely important for a form birefringence to manifest. We, thus, conjecture that the birefringence arises from the phospholipid content of the membrane and that the birefringence variation is a result of the curvature of the membrane, which determines relative molecular orientations.

A positive birefringence has been measured for phospholipid bilayers of a molecular structure close to the bilayers in the RBC membrane.[25] Multiplying an average diameter of the dimple region of the RBC as measured by us with the reported birefringence values measured for various types of phosphatidylcholine bilayers as reported in Ref. 25 gives a range of retardations from ~2 to 33 nm. Considering that phosphatidylcholine is only one of the four phospholipids present in the RBC membrane,[6] the measured retardation is in reasonable agreement with our estimate of the RBC birefringence. Therefore, it is reasonable to conjecture that the origin of the birefringence in the RBC is from the phospholipid content of its cell membrane.

3.5 *Computation of Phospholipid Molecule Contribution to Birefringence*

Here we describe a numerical computation that we have used to validate our conjecture that the birefringence measured in the RBC is due to the phospholipid content in the RBC membrane and that the variation in the birefringence over the volume of the RBC (measurable at the dimple and below detection levels at the rim) is due to the curvature in the RBC membrane.

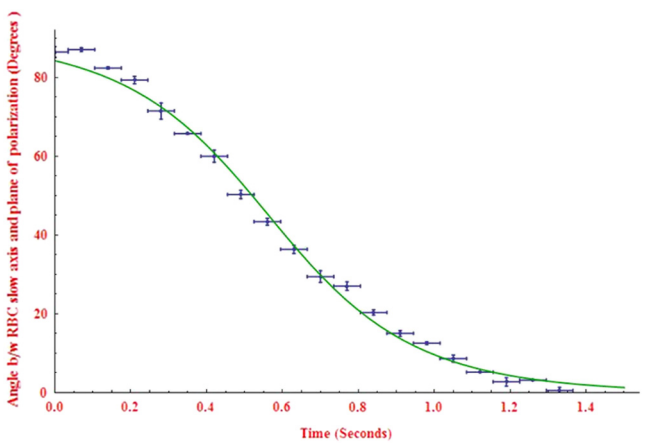

Fig. 8 Variation of angular displacement with time for the process of realignment of the slow axis of an RBC (trapped at 28 mW of laser power) with the laser beam polarization direction in an optical trap. The continuous line is a fit to this data generated using Eq. (2).

To do this, we first construct a simple geometrical model for the RBC surface (Fig. 9). We use the standard values of 8 μm for the diameter of the RBC, and 1 and 2 μm for its minimum and maximum thicknesses, respectively. For the average diameter of the dimple region, we use a value of 5 μm as measured by us in the laboratory. Assuming that the surface of the RBC has no abrupt features like discontinuous changes in its radius of curvature except at the region of transition between the dimple and the rim (Fig. 9), we calculate a value of 8.63 μm as the radius of curvature for the membrane at the dimple region (R_{dimple}) and a value of 1 μm for the radius of curvature at the rim (R_{rim}).

We assume that the lipid molecules are ordered with their long axes perpendicular to the surface of the RBC membrane.[26] We then proceed to study how the change in the orientation of the lipid molecules affects the birefringence measured over a certain region of the specimen. As we have been able to observe birefringence only at the dimple region of the RBC, we carry out our numerical computation over two regions of the RBC membrane: (1) the dimple region, where the surface is essentially like a section of a hollow sphere of radius 8.63 μm with a chord length of 5 μm, and (2) the rim region, where the surface is like a part torus (Fig. 9).

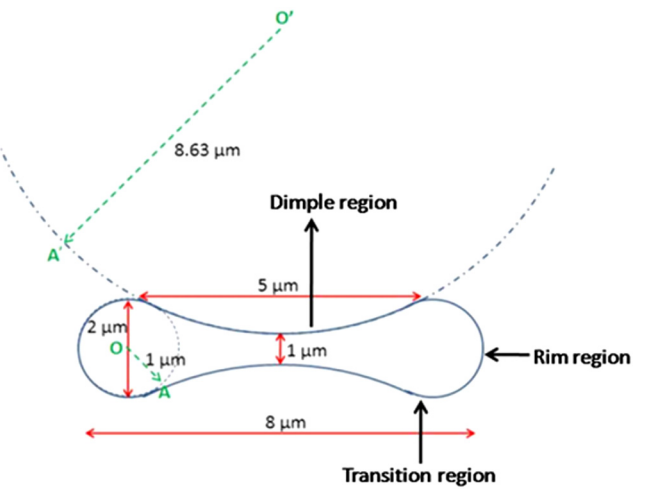

Fig. 9 Geometric model of the human RBC surface: a cross-sectional view. The model is constructed using experimentally measured values of the diameter of the RBC, $D_{\text{RBC}} = 8$ μm, the maximum thickness, $t_{\text{max}} = 2$ μm, the minimum thickness, $t_{\text{min}} = 1$ μm, and the diameter of the dimple, $D_{\text{Dimple}} = 5$ μm. The radius of curvature at the rim (R_{Rim}) is taken to be $t_{\text{max}}/2$, i.e., $R_{\text{Rim}} = \text{OA} = 1$ μm, and the radius of curvature at the dimple ($R_{\text{Dimple}} = \text{O}'\text{A}'$) is found to be 8.63 μm.

The calculations are done assuming only a single layer of the phospholipid molecules at the RBC surface. The transition region between the dimple and the rim, assumed by us to be between radial distances of 2.4 and 2.6 μm, is ignored in all our calculations. This will be a region of very rapid change in the orientation angles of the phospholipid molecules and perhaps also a region of high stress where the equilibrium molecular separation assumed otherwise is unlikely to hold. Any functional form that we can assign to the change in molecular orientation in this region will be without the possibility of experimental verification. As the number of molecules in this region will be only a minute fraction of the total number of molecules that are being considered, ignoring this region in our calculations will not affect the final conclusions.

We follow a method to theoretically correlate the molecular polarizability tensor and the molecular shape factor to the anisotropic refractive indices and, thus, the birefringence as outlined by Salamon and Tollin[26] in their report on using coupled plasmon waveguide resonance measurements to estimate molecular orientation, polarizability, and shape. The method described by Salamon and Tollin is in itself based on the work of Bragg and Pippard[27] on the contribution of molecular shape either as individuals or in molecular aggregates on the form birefringence. Optical anisotropy can arise from either the anisotropy in the molecular polarizability tensor or the asymmetry in the molecular shape factors or both. The relation among the anisotropic refractive indices, the components of the molecular polarizability tensor, and the molecular shape factors is given by

$$(n_i)^2 - 1 = \frac{4\pi\alpha_i}{(V - \alpha_i L_i)}, \tag{3}$$

where n_i is the refractive index, α_i is the ii-component of the polarizability tensor whose principal axes are assumed to coincide with the x, y, and z axes, V is the molecular volume, and L_i is the molecular shape factor. To calculate the molecular shape factors, the long acyl chains in the lipid molecules are represented as cylindrical cavities. Now, if the optical axis of this uniaxially anisotropic medium coincides with the cylinder axis and the electric field is applied in the direction either parallel to this axis or normal to it, the shape factors can be given as[26]

$$L_z = 4\pi\left[1 - \frac{l}{(d^2 + l^2)^{1/2}}\right], \tag{4}$$

$$L_x = \frac{2\pi l}{(d^2 + l^2)^{1/2}}, \tag{5}$$

where l represents the average length of the acyl chains and d is the diameter of the cylinder. If there is a distribution in the molecular orientation (θ), the α_i in Eq. (3) has to be replaced with an average value of the polarizability $[(\alpha_i)_{\mathrm{av}}]$ and L_i with an average value of the shape factor. For the uniaxial lipid molecules, we write $\alpha_x = \alpha_y = \alpha_t$, the transverse polarizability, and $\alpha_z = \alpha_l$, longitudinal polarizability of the lipid molecule, and we have

$$(\alpha_z)_{\mathrm{av}} = \alpha_{\mathrm{av}} + \frac{2}{3}(\alpha_l - \alpha_t)S, \tag{6}$$

$$(\alpha_x)_{\mathrm{av}} = \alpha_{\mathrm{av}} + \frac{1}{3}(\alpha_l - \alpha_t)S, \tag{7}$$

where

$$\alpha_{\mathrm{av}} = \frac{1}{3}(\alpha_l + 2\alpha_t), \tag{8}$$

and S is the degree of orientational order given by

$$S = \frac{1}{2}(3\langle\cos^2\theta\rangle - 1). \tag{9}$$

$\langle\rangle$ represents an average over all orientations. The average shape factors are given by replacing l with $l\cos\theta$ and d with $(d^2/\cos\theta)^{1/2}$, and averaging over all orientations. Thus, we get

$$(n_z)^2 - 1 = \frac{4\pi(\alpha_z)_{\mathrm{av}}}{[V - (\alpha_z)_{\mathrm{av}}(L_z)_{\mathrm{av}}]}, \tag{10}$$

$$(n_x)^2 - 1 = \frac{4\pi(\alpha_x)_{\mathrm{av}}}{[V - (\alpha_x)_{\mathrm{av}}(L_x)_{\mathrm{av}}]}, \tag{11}$$

and using Eqs. (10) and (11), we get the birefringence

$$\Delta n = (n_z - n_x) = \frac{4\pi}{2n_0}\left\{\frac{(\alpha_z)_{\mathrm{av}}}{[V - (\alpha_z)_{\mathrm{av}}(L_z)_{\mathrm{av}}]} - \frac{(\alpha_x)_{\mathrm{av}}}{[V - (\alpha_x)_{\mathrm{av}}(L_x)_{\mathrm{av}}]}\right\}, \tag{12}$$

where $n_0 = (n_z + n_x)/2$ is the average refractive index of the material.

We use the values of transverse and longitudinal polarizabilities as well as the dimensions of the molecules of 1-palmitoyl-2-oleoyl-sn-glycero-3-phosphocholine as given in Ref. 26 for our calculations. We generate S, $(L_z)_{\mathrm{av}}$, and $(L_x)_{\mathrm{av}}$ averaged over all molecular orientations present in the dimple region of the RBC and the same quantities averaged over all molecular orientations present in the rim (see the Appendix for details). Using these and taking an arbitrary value of 1 for n_0, we evaluate the birefringence in the two regions. We get a value of 0.265 in the dimple region and a value of 0.138 in the rim region. Thus, these numerical calculations show that the birefringence arising out of the anisotropic polarizabilities and shape factors of a sample lipid molecule averaged over molecular orientations at the rim region of the RBC is about half of that at the dimple region of the RBC. Given that the birefringence measured at the dimple region is low, it is possible that the still weaker birefringence at the rim is below the detection threshold of our measurement apparatus. Thus, the difference in the membrane curvature at the dimple and the rim regions of the RBC can explain the varying birefringence measurement observed over the RBC volume.

We have also presented the variation in the computed value of the birefringence when averaging over all molecular orientations present on the RBC membrane enclosed within a projected circular area with the radius of this circle as it is made to vary from the geometric center of the RBC along a diametric line to the radius of the RBC [Fig. 10(a)] (see the Appendix for details). For the reasons given above, we have not plotted the values in the transition region. We find that there is a steady drop in the birefringence value in the dimple region as molecules with larger tilts to the normal to the plane of the RBC are included

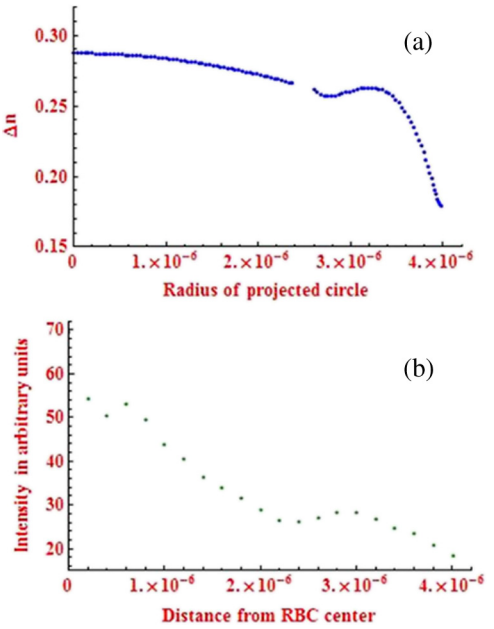

Fig. 10 (a) Plot of numerically computed birefringence due to all phospholipid molecular orientations present on the RBC membrane within a projected circular area as a function of the radius of this area. The discontinuity seen in the plot is due to the fact that computations in the transition region between 2.4 and 2.6 μm have not been carried out. (b) Variation of experimentally measured intensity with distance from center of RBC that is oriented edge-on to beam propagation direction between crossed polarizers in a polarizing microscope.

with an increase in the radial distance. At the start of the rim, we see an initial rise in the birefringence value with radial distance as there is now an inclusion of molecules with progressively smaller tilt angles to the normal to the plane of the RBC. A sharp fall in the value of the birefringence follows this.

Figure 10(b) shows the intensity profile along a diametric line of the RBC when viewed edge-on between crossed polarizers under green light illumination. Note the presence of the shoulder like feature flanking the main peak in the intensity variation with radial distance. This variation of intensity being proportional to the birefringence shows a trend similar to the variation of the birefringence itself, thus lending further support to our hypothesis that the phospholipid content of the RBC membrane can explain the birefringence values measured over the RBC volume. We note here that birefringence measurements are sensitive to curvature changes in the RBC membrane.

3.6 *Birefringence of RBCs that are Shape Restored Subsequent to Crenation*

The contraction of a cell into a scalloped structure due to exosmosis of water on exposure to a solution that is either hypertonic or with pH altered toward acidic conditions is called crenation. It has been reported in the literature that the initial stages of crenation in an RBC are completely reversible.[28] We refer to RBCs that are reformed in shape consequent to a process of crenation as reformed RBCs. The elasticity of the cell membrane of an RBC is affected by the process of crenation as has been reported in Ref. 23. The cell membrane of the reformed RBCs correspond to a much lower shear modulus as compared to normal RBCs. This affects their dynamics in the optical tweezer in terms of a longer time required for acquiring an edge-on orientation to the incoming laser beam. In addition, it was observed that there is a sluggish response to aligning themselves about an axis that coincided with the polarization direction. This suggests that the slow axis that aligns parallel to the polarization vector was no longer realized along every diameter of the restored cell. Thus, shape restoration seems to result in perturbing the symmetry of the dimple region, rendering some of the directions along the diameters ineffectual as slow axes. In concomitant measurements with the polarizing microscope, the retardation measured was found to be lower than that of normal RBCs, and in some cells, even absent. As the process of crenation can alter the alignment of phospholipids in the RBC membrane, the reduced and sometimes absent birefringence measured is in agreement with our conjecture that the birefringence of the RBC arises from the phospholipid content of the cell membrane. We note here that any process that affects the cell membrane in terms of the alignment of the phospholipid molecules in it will affect the birefringence of the RBC as well as the optomechanical response of the RBC in a trap.

3.7 *Birefringence of Chicken Red Blood Cell*

In order to underscore the role of the cell membrane contour in determining the variation in birefringence over the surface of the cell, we report here results of studies that we have carried out on a particular example of avian red blood cells, namely that of broiler chicken (biological name Gallus gallus domesticus). Unlike human red blood cells, chicken red blood cells are nucleated and have an oblong shape with an average length of ~11.9 μm and a width of ~7.1 μm.[29] Under a microscope, chicken erythrocytes appear ellipsoidal in shape. We did not find any reports on the thickness of chicken erythrocytes. However, images recorded by us in the polarizing microscope suggest that the thickness varies over the surface of the chicken RBC with a pronounced bulge over the central region that houses the cell nucleus. This is like a contrasting counterpart of the dimple region of the human RBC.

Using a polarizing microscope, we have identified the long axis of the oblong to be the slow axis. Figure 11(a) shows the intensity profile of chicken RBCs in an edge-on orientation when viewed under crossed polarizers in a polarizing microscope. The intensity profile is in clear contrast to the case of human RBCs. While in human RBCs the intensity is maximum in the center of the dimple region decreasing toward its edges and falling below detection limits in the rim, here the intensity is below detection limits at the central region. The central dark region is observed to be flanked on either side by an intensity

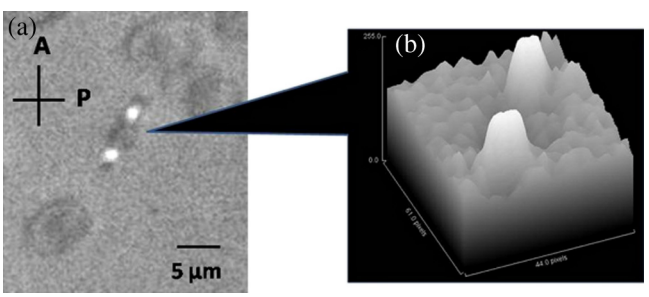

Fig. 11 (a) Chicken RBC in edge-on orientation between crossed polarizers and green light ($\lambda = 546$ nm) illumination. (b) Surface intensity plot of the freely suspended chicken RBC.

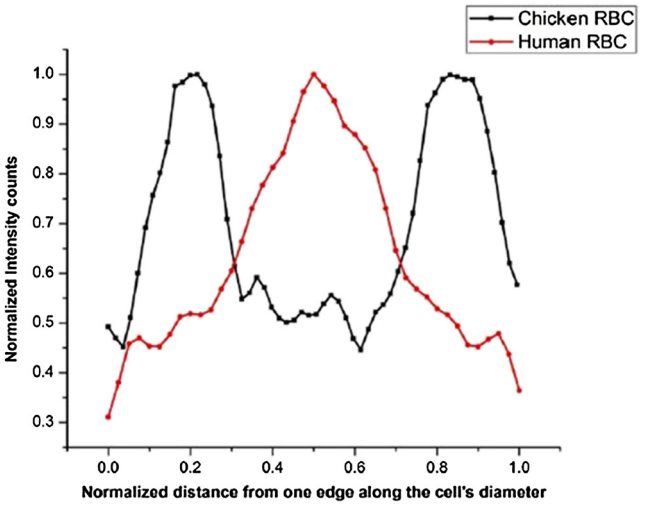

Fig. 12 Comparison of intensity profiles for human and chicken RBCs under crossed polarizers.

peak. Figure 11(b) shows the variation of intensity over the surface of the chicken RBC in an edge-on orientation, while Fig. 12 shows the variation of the intensity along the long axis of the chicken RBC. The separation in the two maxima in the intensity variation (estimated to be $\sim$7.9 μm from the intensity variation pattern) is well beyond the largest dimension of the cell nucleus dimension ($\approx$4.2 μm) as estimated from our microscope images. The value of retardation, as measured by the Sénarmont technique, was found to be in the same range as that of the human RBCs. As cell membranes, in general, are made up of a phospholipid bilayer[30] and owing to the fact that the value of retardation measured here is comparable to that of a human RBC, we conjecture that in the case of chicken erythrocytes, the birefringence is primarily due to the phospholipid content of the cell membrane as well. The variation of intensity over the chicken RBC surface when viewed under crossed polarizers in a polarizing microscope is, therefore, also due to the variation in curvature of the membrane surface, which in turn affects the relative orientations of the phospholipid molecules. As the central bulge is the region of maximum rate of change in the phospholipid molecule orientations, the birefringence measured here is minimal. In the relatively flat flanking region, where the relative orientations of the phospholipid molecules do not change very rapidly, a higher intensity is measured [Figs. 11(b) and 12]. It is, thus, clear that birefringence measurements are indeed very sensitive to cell membrane curvature.

It is essential for us to develop a plausible mathematical model for the cell membrane curvature in a chicken RBC before a numerical computation of the birefringence can be attempted. The lack of circular symmetry as compared to the human RBC will make this more challenging. Further, it would be interesting to study the optomechanical response of chicken RBCs in an optical tweezer where the shape asymmetry and nonequivalence of all major axes as slow axes could lead to intriguing results. Maximization of the cell volume in the region of highest electric field would dictate that the chicken RBC orients itself with the long axis parallel to the beam propagation direction. On the other hand, alignment of the slow axis with the direction of polarization of the laser would require that the orientation is such that the long axes are perpendicular to the beam direction.

4 Conclusions

A normal human RBC is rotationally bound to the direction of the electric field vector in a linearly polarized tweezer establishing that it is birefringent. We have quantified this birefringence and identified the slow axis to be along a diameter of the cell. This estimate of the birefringence is in agreement with what we can calculate from optical tweezer experiments. We find that the birefringence is confined to the dimple region of the RBC.

Constituents of the RBC cytoplasm, especially hemoglobin, are uniformly spread over the RBC volume and, thus, we expect to find it in greater quantity at the rim rather than at the dimple and, hence, cannot associate the birefringence with it. Phospholipid bilayers of molecular structure close to the bilayers found in the RBC have been shown to exhibit birefringence.[25] Using the values of birefringence measured for these phospholipids and the optical path length in the RBC, we find that the values of retardation are in the same range as what we measure for the RBC. We, therefore, conjecture that the birefringence we measure arises from the phospholipid content of the RBC cell membrane and the variation seen over the RBC volume is a consequence of the molecular alignment in the phospholipid bilayer, which is linked to the curvature of the membrane. The membrane curvature is a minimum at the dimple region of the RBC and the phospholipids in this region are, therefore, maximally aligned. The situation is different at the outer edges of the cell where the light samples a wider range of orientations of the phospholipids, with the membrane curvature here being greater. This leads to a contrast in the measured birefringence of the two regions. We have constructed a simple geometric model for the RBC membrane surface and have carried out computations of birefringence that can be expected for molecular orientations of a sample phospholipid molecule assumed to be oriented normally to the local surface tangent over such a surface. We find that the variation in the measured values of birefringence is in agreement with our computation. We note here that the enhanced birefringence at the dimple region could also arise due to the close proximity of the aligned phospholipid molecules of the two opposing membranes, an effect that our model does not incorporate in its present form. Nonetheless, membrane curvature linked changes in the molecular alignment in the phospholipid layer are clearly seen in the birefringence measurement.

In order to endorse the role of the phospholipid content of the membrane and the relative molecular orientations as brought about by the membrane curvature in explaining the origin of birefringence as well as its variation over the cell surface, we have compared the results of our studies on reformed human RBCs and chicken RBCs with that of human RBCs. Our studies with reformed human RBCs have established that damage to the RBC membrane has clear signatures in the birefringence measurement. An earlier study has already shown that the process of shape reforming an RBC after crenation affects the membrane elasticity.[23] We have shown with this study that this process also results in reduced or sometimes absent birefringence, which links up with the sluggish reorientation and alignment response in a linearly polarized optical tweezer. In the case of the chicken RBC, the cell is oblong and nucleated and has a membrane contour completely unlike that of a human RBC. Notably, there is a pronounced bulge at the center, in contrast to the dimple region of the human RBC and has rapidly changing relative molecular orientations in this region as compared to the flanking regions. The birefringence over the cell surface is indeed in conformity

with being the least where relative phospholipid molecular orientations change rapidly and highest where the relative orientations hardly change. Again, we note here that variation in the birefringence over the chicken RBC function could be a function of the proximity of the aligned phospholipid molecules forming the membrane on either side of the cell leading to an enhancement when they are close, as in the edges, and very low values in the central region, where they are farther apart due to the presence of the nucleus. We also note here that if the origin of the birefringence in these cells is thought to arise from a partially aligned subpopulation of hemoglobin molecules, it will, nonetheless, be impossible to ignore the role of the membrane contour in aligning these molecules in order to consistently explain the results for all the three cases that we have discussed here.

We reemphasize here that while birefringence has been reported in the human RBC earlier, the source of this effect was tied to either distortions in the cell shape or abnormalities in the hemoglobin content. There is only one study where birefringence is reported in an undistorted normal human RBC, but the cause of this was attached to the probable presence of protein chains at the dimple region that ran across the thickness of the cell connecting opposite sides of the RBC membrane.[15] Later studies of the structure of the RBC have ruled out the presence of such protein chains.[6,11] We have shown here that the current knowledge of the RBC membrane structure can explain the differential birefringence measured over the volume of an undistorted normal human RBC. We have also tied the birefringence measurement of the RBC consistently with its optomechanical properties as observed in an optical tweezer. Our results on the restored RBCs show that changes in the physiological conditions of the RBC are reflected in the birefringence measurement. We have also shown that the birefringence data contain information with regard to subtle changes in the membrane structure in terms of change in the orientation of the constituent phospholipid molecules. It is even possible to gauge the boundaries of the dimple region of the RBC from such a measurement. Thus, monitoring variations of birefringence both spatially and temporally could open up newer ways of understanding the structure and dynamics of the RBC membrane.

Appendix: Computation of Human RBC Cell Membrane Phospholipid Contribution to Birefringence

Let d be the diameter of a single phospholipid molecule, R_{Dimple} and R_{Rim} be the radii of curvature at the dimple and rim regions of the RBC, respectively, and D_{RBC} and D_{Dimple} be the diameters of the RBC and the dimple region of the RBC, respectively. In the dimple region, the orientation of a phospholipid molecule located at an arc length of OX from the geometric center of the RBC is given by

$$\theta(n) = \frac{\mathrm{OX}}{R_{\mathrm{Dimple}}} = \frac{nd}{R_{\mathrm{Dimple}}}, \tag{13}$$

where n is a positive integer, while the number of molecules having such an orientation is given by

$$N[\theta(n)] = \frac{1}{d} 2\pi R_{\mathrm{Dimple}} \sin[\theta(n)]. \tag{14}$$

Further, the variation of θ in the dimple region will be from 0 deg to θ_{fD} such that

$$R_{\mathrm{Dimple}} \sin[\theta(n)] = \frac{D_{\mathrm{Dimple}}}{2}. \tag{15}$$

However, as we do not wish to carry out the computation in the transition region from the dimple region of the RBC to the rim, we compute a final value for n in the dimple region (n_{fD}) that is given by

$$n_{fD} = \frac{1}{d} R_{\mathrm{Dimple}} \sin^{-1}\left(\frac{2.4\ \mu\mathrm{m}}{R_{\mathrm{Dimple}}}\right). \tag{16}$$

Now, we compute values of S, L_z, and L_x for radial distances varying from 0 to $D_{\mathrm{Dimple}}/2$ using the following expressions:

$$N_{\mathrm{tot}}(n_D) = \sum_{n=0}^{n_D} N[\theta(n)], \tag{17}$$

$$S(n_D) = \frac{1}{2}\left\{3\frac{\sum_{n=0}^{n_D} N[\theta(n)]\cos^2[\theta(n)]}{N_{\mathrm{tot}}(n_D)} - 1\right\}, \tag{18}$$

$$L_z(n_D) = \frac{1}{N_{\mathrm{tot}}(n_D)} \sum_{n=0}^{n_D} N[\theta(n)] 4\pi \times \left\{1 - \frac{l\cos[\theta(n)]}{\sqrt{\frac{d^2}{\cos[\theta(n)]} + l^2\cos^2[\theta(n)]}}\right\}, \tag{19}$$

$$L_x(n_D) = \frac{1}{N_{\mathrm{tot}}(n_D)} \sum_{n=0}^{n_D} N[\theta(n)] \frac{2\pi l\cos[\theta(n)]}{\sqrt{\frac{d^2}{\cos[\theta(n)]} + l^2\cos^2[\theta(n)]}}, \tag{20}$$

for n_D varying from 0 to n_{fD}. Substituting values of $S(n_D)$, $L_z(n_D)$, and $L_x(n_D)$ in Eq. (12), we get $\Delta n(n_D)$ and plot it as a function of radial distance, R_{dist}, given by

$$R_{\mathrm{dist}} = 2\pi R_{\mathrm{Dimple}} \sin[\theta(n_D)] \tag{21}$$

in Fig. 10(a). The value of $\Delta n(n_D = n_{fD})$ gives us the birefringence on averaging over all phospholipid orientations present in the entire dimple region of the RBC.

For the rim region, the orientation of the phospholipid molecule with respect to the normal to the plane of the RBC is given by

$$\theta_R(n) = \left|\theta_{iR} - \frac{nd}{R_{\mathrm{Rim}}}\right|, \tag{22}$$

where θ_{iR} is the initial angle of orientation in the rim region given by

$$\theta_{iR} = \sin^{-1}\left(\frac{\frac{D_{\mathrm{RBC}}}{2} - \frac{D_{\mathrm{Dimple}}}{2} - R_{\mathrm{Rim}}}{R_{\mathrm{Rim}}}\right), \tag{23}$$

while n is a positive integer. Once again, as we do not wish to carry out the computation in the transition region from the dimple region of the RBC to the rim, we compute an initial value for n in the dimple region (n_{iR}), which is given by

$$n_{iR} = \frac{R_{\mathrm{Rim}}}{d}\left[\sin^{-1}\left(\frac{0.5\ \mu\mathrm{m}}{R_{\mathrm{Rim}}}\right) - \sin^{-1}\left(\frac{0.4\ \mu\mathrm{m}}{R_{\mathrm{Rim}}}\right)\right]. \tag{24}$$

Also, defining the quantity

$$\theta'_R(n) = \left(\theta_{iR} - \frac{nd}{R_{\mathrm{Rim}}}\right), \tag{25}$$

we get the number of phospholipid molecules having an orientation of $\theta_R(n)$ from the expression

$$N_R[\theta_R(n)] = \frac{1}{d}2\pi\left\{\frac{D_{\mathrm{RBC}}}{2} - R_{\mathrm{Rim}} - R_{\mathrm{Rim}}\ \sin[\theta'_R(n)]\right\}. \tag{26}$$

In the rim, the variation of the orientation is from θ_{iR} to $\theta_{fR} = \theta_{iR} + \pi/2$, thus yielding a final value for n in the rim region, n_{fR}, using Eq. (22). We can now continue computing values of S, L_z, and L_x for all orientations of the phospholipid molecules present on the RBC membrane enclosed within a projected circular area of radius (radial distance)

$$R_{\mathrm{dist}} = \frac{D_{\mathrm{RBC}}}{2} - R_{\mathrm{Rim}} - R_{\mathrm{Rim}}\ \sin[\theta'_R(n)] \tag{27}$$

using the following expressions:

$$N_{R\mathrm{tot}}(n_R) = \sum_{n=n_{iR}}^{n_D} N_R[\theta_R(n)], \tag{28}$$

$$S_R(n_R) = \frac{1}{2}\left(\frac{3}{N_{\mathrm{tot}}(n_{fD}) + N_{Rtot}(n_R)}\left\{N_{\mathrm{tot}}(n_{fD})S(n_{fD}) + \sum_{n=n_{iR}}^{n_R} N_R[\theta_R(n)]\cos^2[\theta'_R(n)]\right\} - 1\right), \tag{29}$$

$$L_{z(R)}(n_R) = \frac{1}{N_{\mathrm{tot}}(n_{fD}) + N_{R\mathrm{tot}}(n_R)}\left(N_{\mathrm{tot}}(n_{fD})L_z(n_{fD}) + \sum_{n=n_{iR}}^{n_R} N_R[\theta_R(n)]4\pi \times\left\{1 - \frac{l\ \cos[\theta_R(n)]}{\sqrt{\frac{d^2}{\cos[\theta_R(n)]} + l^2\cos^2[\theta_R(n)]}}\right\}\right), \tag{30}$$

$$L_{x(R)}(n_R) = \frac{1}{N_{\mathrm{tot}}(n_{fD}) + N_{R\mathrm{tot}}(n_R)}\left\{N_{\mathrm{tot}}(n_{fD})L_x(n_{fD}) + \sum_{n=n_{iR}}^{n_R} N_R[\theta_R(n)]\frac{2\pi l\cos[\theta_R(n)]}{\sqrt{\frac{d^2}{\cos[\theta_R(n)]} + l^2\cos^2[\theta_R(n)]}}\right\}, \tag{31}$$

for n_R varying from n_{iR} to n_{fR}. These values are then substituted in Eq. (12) to generate $\Delta n(n_R)$, which has then been plotted in Fig. 10(a) as a function of the radial distance. The birefringence when averaging over all molecular orientations present in the rim region alone can be derived from Eqs. (26)–(31) by ignoring the contribution from the dimple region and modifying the number of molecules in the denominator appropriately. Explicitly, the expressions are

$$S_{\mathrm{Rim}} = \frac{1}{2}\left\{\frac{3}{N_{R\mathrm{tot}}(n_{fR})}\sum_{n=n_{iR}}^{n_{fR}} N_R[\theta_R(n)]\cos^2[\theta'_R(n)] - 1\right\}, \tag{32}$$

$$L_{z(\mathrm{Rim})} = \frac{1}{N_{R\mathrm{tot}}(n_{fR})}\left(\sum_{n=n_{iR}}^{n_{fR}} N_R[\theta_R(n)]4\pi \times\left\{1 - \frac{l\ \cos[\theta_R(n)]}{\sqrt{\frac{d^2}{\cos[\theta_R(n)]} + l^2\cos^2[\theta_R(n)]}}\right\}\right), \tag{33}$$

$$L_{x(\mathrm{Rim})} = \frac{1}{N_{R\mathrm{tot}}(n_{fR})}\left\{\sum_{n=n_{iR}}^{n_{fR}} N_R[\theta_R(n)] \times\frac{2\pi l\ \cos[\theta_R(n)]}{\sqrt{\frac{d^2}{\cos[\theta_R(n)]} + l^2\cos^2[\theta_R(n)]}}\right\}, \tag{34}$$

which can be substituted in Eq. (12) to get the birefringence value on averaging over phospholipid molecular orientations present in the rim region of the RBC alone.

Acknowledgments

The authors thank N. V. Madusudhana, Vivek Revanakar, and S. A. Rangwala for useful discussions, Sharath R. for his help in preparing some of the samples, Dr. Veere Gowda for kind provision of avian red blood cells, and Rekha S. for help with the analysis work. This work was enabled through a grant from the Department of Science and Technology, Government of India, under the Nano Mission.

References

1. Y. Park et al., "Measurement of the nonlinear elasticity of red blood cell membranes," *Phys. Rev. E* **83**(5), 051925 (2011).
2. Y. Park et al., "Measurement of red blood cell mechanics during morphological changes," *Proc. Natl. Acad. Sci.* **107**, 6731–6736 (2010).
3. M. De Oliveira et al., "Nanomechanics of multiple units in the erythrocyte membrane skeletal network," *Ann. Biomed. Eng.* **38**, 2956–2967 (2010).
4. Y. Park et al., "Metabolic remodeling of the human red blood cell membrane," *Proc. Natl. Acad. Sci.* **107**, 1289–1294 (2010).
5. J. Evans et al., "Fluctuations of the red blood cell membrane: relation to mechanical properties and lack of ATP dependence," *Biophys. J.* **94**, 4134–4144 (2008).

6. N. Mohandas and P. G. Gallagher, "Red cell membrane: past, present, and future," *Blood* **112**, 3939–3948 (2008).
7. J. Li et al., "Cytoskeletal dynamics of human erythrocyte," *Proc. Natl. Acad. Sci.* **104**(12), 4937–4942 (2007).
8. Y. P. Liu, C. Li, and A. C. K. Lai, "Experimental study on the deformation of erythrocytes under optically trapping and stretching," *Mater. Sci. Eng.* **423**, 128–133 (2006).
9. T. M. Fischer, "Shape memory of human red blood cells," *Biophys. J.* **86**, 3304–3313 (2004).
10. M. Dao, C. T. Lim, and S. Suresh, "Mechanics of the human red blood cell deformed by optical tweezers," *J. Mech. Phys. Solids* **51**, 2259–2280 (2003).
11. G. B. Ralston, "The structure of spectrin and the shape of the red blood cell," *Trends Biochem. Sci.* **3**(3), 195–198 (1978).
12. E. Higurashi, R. Sawada, and T. Ito, "Optically induced angular alignment of trapped birefringent micro-objects by linearly polarized light," *Phys. Rev. E* **59**(3), 3676–3681 (1999).
13. M. E. J. Freise et al., "Optical alignment and spinning of laser-trapped microscopic particles," *Nature* **394**, 348–350 (1998).
14. J. Cheng, P. M. Chaikin, and T. G. Mason, "Light streak tracking of optically trapped thin microdisks," *Phys. Rev. Lett.* **89**(10), 108303 (2002).
15. B. B. Srivastav and A. C. Burton, "Evidence from studies of birefringence of structure across the dimple region of red cells," *J. Cell. Physiol.* **74**, 101–114 (1969).
16. M. F. Perutz and J. M. Mitchison, "State of haemoglobin in sickle-cell anaemia," *Nature* **166**, 677–679 (1950).
17. E. Ponder and D. Barreto, "The birefringence of the human red cell ghosts," *J. Gen. Physiol.* **39**(3), 319–324 (1956).
18. J. M. Mitchison, "Thickness and structure of the membrane of the human red cell ghost," *Nature* **166**, 347–348 (1950).
19. A. Ghosh et al., "Euler buckling-induced folding and rotation of red blood cells in an optical trap," *Phys. Biol.* **3**, 67–73 (2006).
20. M. W. Kaplan, "Birefringence in biological materials," *Proc. SPIE* **112**, 112–119 (1977).
21. A. Rich, "Use of the Sénarmont compensator for measuring double refraction of flow," *J. Opt. Soc. Am.* **45**(5), 393–394 (1955).
22. V. Twersky, "Birefringence and dichroism," *J. Opt. Soc. Am.* **71**(10), 1243–1249 (1981).
23. P. Parthasarathi et al., "Orientational dynamics of human red blood cells in an optical trap," *J. Biomed. Opt.* **18**(2), 025001 (2013).
24. N. Mohandas and E. Evans, "Mechanical properties of the red cell membrane in relation to molecular structure and genetic defects," *Annu. Rev. Biophys. Biomol. Struct.* **23**(1), 787–818 (1994).
25. J. J. Ramsden, "Molecular orientation in lipid bilayers," *Philos. Mag. B* **79**(3), 381–386 (1999).
26. Z. Salamon and G. Tollin, "Optical anisotropy in lipid bilayer membranes: coupled plasmon-waveguide resonance measurement of molecular orientation, polarisability and shape," *Biophys. J.* **80**, 1557–1567 (2001).
27. W. L. Bragg and A. B. Pippard, "The form birefringence of macromolecules," *Acta Crystallogr.* **6**, 865–867 (1953).
28. M. M. Gedde, E. Yang, and W. H. Huestis, "Shape response of human erythrocytes to altered cell pH," *Blood* **86**(4), 1595–1599 (1995).
29. S. Nowaczewski and H. Kontecka, "Haematological indices, sizes of erythrocytes and haemoglobin saturation in broiler chicken kept in commercial conditions," *Anim. Sci. Pap. Rep.* **30**(2), 181–190 (2012).
30. B. Alberts et al., *Molecular Biology of the Cell*," 4th ed., Garland Science, New York (2002).

Belavadi Venkatakrishnaiah Nagesh works as an assistant professor at the M S Ramaiah Institute of Technolgy, Bangalore. He received his master's degree in physics from Kuvempu University, Karanataka. He is currently pursuing his doctoral degree under Prof. Sharath Ananthamurthy at the Department of Physics, Bangalore University, Bangalore, in the field of soft condensed matter.

Yogesha is currently working as an assistant professor at the Government Science College, Hassan, Karnataka, India. He received his master's degree in physics in 2004 from the University of Mysore. He received his doctoral degree from Bangalore University in 2013 under the guidance of Prof. Sharath Ananthamurthy. His research interests include rheology of materials and soft condensed matter.

Pratibha Ramarao is currently working as an associate professor in the soft condensed matter lab of the Raman Research Institute, Bangalore, India. Her research interests include studies on phase transitions, defects, electro-optic switching, and field induced effects in unconventional liquid crystals with reduced symmetry. Dielectric spectroscopy of polyelectrolytes is another field of current interest.

Praveen Parthasarathi received his master's degree in physics in 2008 from Bangalore University, Bangalore. He is currently pursuing his doctoral degree under Prof. Sharath Ananthamurhy at the Department of Physics, Bangalore University, Bangalore. His research interests include physics of optical tweezers and soft condensed matter.

Shruthi Subhash Iyengar received her master's degree in physics in 2011 from Bangalore University, Bangalore. She is currently pursuing her doctoral degree under Dr. Sarbari Bhattacharya in the Department of Physics, Bangalore University, Bangalore. Her research interests include magnetism and magnetic interactions in soft and living matter.

Sarbari Bhattacharya is a condensed matter physicist by training and has studied magnetic properties of transition metal based metallic glasses, thin films, and nanoparticles for her doctoral and post-doctoral work in India, France, and Germany. She is currently assistant professor at the Department of Physics, Bangalore University, India, where in addition to teaching she pursues research on soft and living matter using optical tweezer based techniques.

Sharath Ananthamurthy is professor and Chair of the Department of Physics at Bangalore University. His MSc in physics was from I.I.T. Kanpur, India, and his PhD from the University of Iowa, USA, in chemical physics. His interests are in applying optical methods, particularly using optical tweezers and Raman spectroscopy, to studying the rheology of soft condensed matter systems. He also carries out research on nonneutral plasmas using ion traps.